# A High-precision Trigonometric Parallax to an Ancient Metal-poor Globular Cluster[*]

T. M. Brown[1] ⬤, S. Casertano[1], J. Strader[2], A. Riess[1,3], D. A. VandenBerg[4], D. R. Soderblom[1], J. Kalirai[1,3], and R. Salinas[5]

[1] Space Telescope Science Institute, 3700 San Martin Drive, Baltimore, MD 21218, USA
tbrown@stsci.edu, stefano@stsci.edu, drs@stsci.edu, ariess@stsci.edu, jkalirai@stsci.edu
[2] Department of Physics and Astronomy, Michigan State University, East Lansing, MI 48824, USA; strader@pa.msu.edu
[3] Department of Physics and Astronomy, Johns Hopkins University, Baltimore, MD 21218, USA
[4] Department of Physics and Astronomy, University of Victoria, P.O. Box 1700, STN CSC, Victoria, BC V8W 2Y2, Canada; vandenbe@uvic.ca
[5] Gemini Observatory, Casilla 603, La Serena, Chile; rsalinas@gemini.edu

## Abstract

Using the Wide Field Camera 3 (WFC3) on the *Hubble Space Telescope* (*HST*), we have obtained a direct trigonometric parallax for the nearest metal-poor globular cluster, NGC 6397. Although trigonometric parallaxes have been previously measured for many nearby open clusters, this is the first parallax for an ancient metal-poor population—one that is used as a fundamental template in many stellar population studies. This high-precision measurement was enabled by the *HST*/WFC3 spatial-scanning mode, providing hundreds of astrometric measurements for dozens of stars in the cluster and also for Galactic field stars along the same sightline. We find a parallax of $0.418 \pm 0.013 \pm 0.018$ mas (statistical, systematic), corresponding to a true distance modulus of $11.89 \pm 0.07 \pm 0.09$ mag ($2.39 \pm 0.07 \pm 0.10$ kpc). The *V* luminosity at the stellar main-sequence turnoff implies an absolute cluster age of $13.4 \pm 0.7 \pm 1.2$ Gyr.

*Key words:* astrometry – globular clusters: general – globular clusters: individual (NGC 6397) – stars: distances – stars: evolution

## 1. Introduction

Stellar populations at all redshifts are interpreted within the framework of stellar evolution models, and the observational foundation for such models are Galactic star clusters, because they provide samples at nearly fixed distance, age, and chemical composition. When employing isochrones to interpret a stellar population, it is common to cite cluster reference points, quoting the ages and metallicities for which the isochrone library best matches observed color–magnitude diagrams (CMDs). For example, the ancient metal-poor anchor in the Bruzual & Charlot (2003) stellar population models is NGC 6397.

There are dozens of open clusters within 1 kpc (Dias et al. 2002), and many have direct parallaxes (e.g., Soderblom et al. 2005; van Leeuwen 2009; van Leeuwen et al. 2017), but the nearest globular clusters are at larger distances that put them beyond the reach of *Hipparcos* or the Fine Guidance Sensor on the *Hubble Space Telescope* (*HST*). This problem has weakened the observational foundation for much of astronomy, because the distances to all metal-poor ([Fe/H] < −1) and ancient (age > 10 Gyr) star clusters have until now been based upon indirect methods, such as main-sequence subdwarf fitting (e.g., Gratton et al. 2003), RR Lyrae (e.g., Cacciari & Clementini 2003), dynamical modeling (e.g., van der Marel & Anderson 2010), and white-dwarf (WD) fitting (e.g., Hansen et al. 2007). Distances to fiducial globular clusters are the largest uncertainty when using them to anchor stellar models.

That situation is now on the verge of dramatic improvement. With the advent of spatial scanning (MacKenty 2012; Riess et al. 2014; Casertano et al. 2016), the nearest globular clusters are

within reach of *HST*, and many more are within reach of *Gaia* (Pancino et al. 2017). The closest is M4—an intermediate-metallicity ([Fe/H] = −1.15; Kraft & Ivans 2003) cluster with an age of 11.5 Gyr (VandenBerg et al. 2013) and highly uncertain distance (1.7–2.2 kpc; e.g., Harris 1996; Hansen et al. 2004; Bedin et al. 2009), due to its unusual foreground reddening. NGC 6397 is the next closest, and a much better template for ancient metal-poor populations. Its distance modulus has been determined by both main-sequence fitting (12.13 mag, Reid & Gizis 1998; 12.01 mag, Gratton et al. 2003) and WD fitting (12.03 mag; Hansen et al. 2007), implying a distance of 2.6 kpc. Independent spectroscopic metallicity measurements give [Fe/H] = −2.03 (Gratton et al. 2003) and −2.02 (Kraft & Ivans 2003), and fitting of the main-sequence turnoff (MSTO) implies an age of 13.0 Gyr (VandenBerg et al. 2013). Its Galactic latitude ($l = 338.17$, $b = −11.96$) facilitates spatial scanning of both cluster and reference field stars of suitable brightness and distance. It is moderately reddened; we assume $E(B − V) = 0.185$ mag, based upon measurements of 0.183 mag (Gratton et al. 2003), 0.186 mag (Schlegel et al. 1998), and 0.187 mag (Anthony-Twarog et al. 1992). NGC 6397 is of moderate luminosity ($M_{Vt} = −6.64$ mag; Harris 1996), and thus much less massive than clusters with complex populations such as NGC 2808 and $\omega$ Cen (e.g., Piotto et al. 2015).

Because of its fundamental importance as a population template, we have obtained *HST* spatial scans of NGC 6397 with the goal of obtaining a high-precision measurement of its trigonometric parallax. We are currently achieving a parallax precision $\sim$20–100 $\mu$as per star, which is competitive with the measurements that will be obtained by *Gaia*. In Gaia Data Release 1, parallaxes for nearby globular clusters are barely detectable (Watkins & van der Marel 2017). Single-star precisions in the upcoming *Gaia* data release are likely to be at the level of 100 $\mu$as (Prusti 2012), and possibly somewhat better. Compared to our measurements, the final *Gaia* parallaxes will have smaller uncertainties for the brightest M
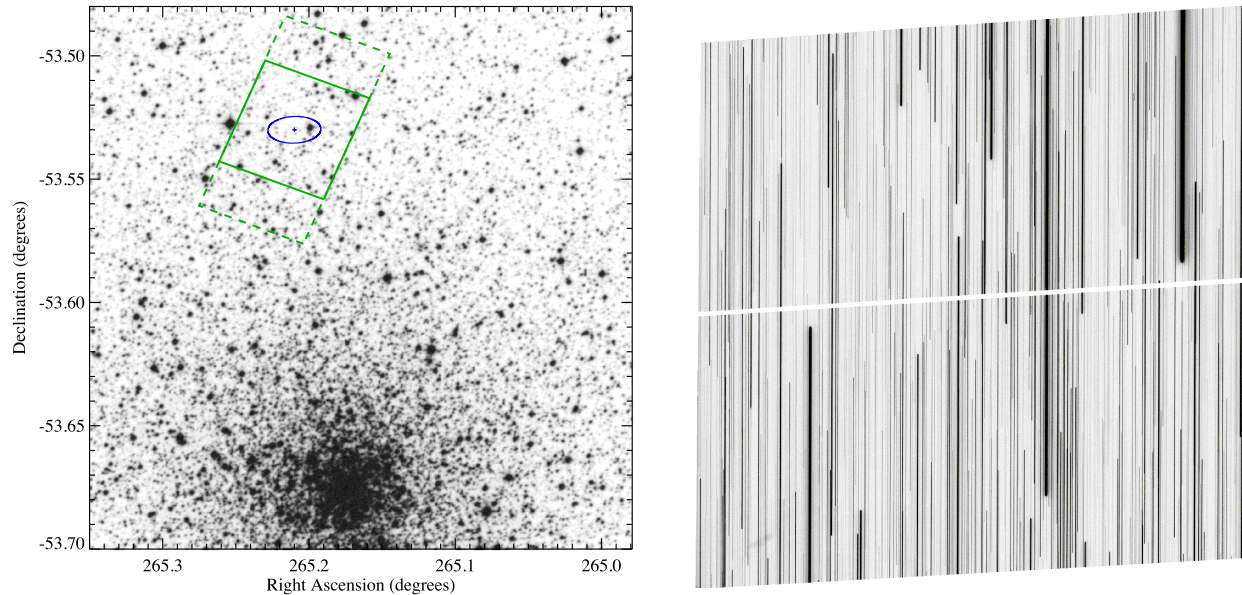
**Figure 1.** Left panel: a Digital Sky Survey image of NGC 6397 showing a simplified WFC3 footprint (solid green) at the center of the area scanned (dashed green). The area and position angle were chosen to maximize the number of bright ($V < 18$ mag) field and cluster stars that could be scanned without neighbor contamination, while maximizing the parallax motion that can be measured within the observing constraints. The parallax ellipse for stars in NGC 6397 (blue) is shown magnified by $10^5$. Our astrometric information is in a single axis, perpendicular to the scan. Right panel: a scan of the NGC 6397 field, shown at a clipped linear stretch.

giants, and larger uncertainties at $V \gtrsim 14$ mag. *Gaia* results rely upon exquisite orientation knowledge for widely separated fields, while *HST* results are based upon precise relative measurements anchored to field reference stars. Given the distinct systematics, our measurement provides an independent check of *Gaia* measurements for this critical cluster. Presently, our uncertainties are dominated by systematic errors, but we continue to improve our analysis, and plan to address these in a future paper. Given our current precision, using a method completely independent from previous distance estimates and upcoming *Gaia* results, it is appropriate to provide a preliminary result at this time.

## 2. Data

### 2.1. HST Observations

We obtained five orbits of WFC3 imaging over the course of 2 years, with one orbit every six months, beginning in 2014 September, timed to occur near the maximum parallactic motion of NGC 6397. A link to the *HST* data is provided here: 10.17909/T9SX1F. Each epoch included four spatial scans in the F606W filter and eight direct images in the F336W, F467M, F547M, and F850LP filters. The spatial scans did not hold a fixed position, but instead trailed the field at $0\rlap{.}''41$ s$^{-1}$ across the detector for 3600 pix along a path that produced trails approximately aligned with the *y*-axis (Figure 1), deviating by $\sim0\rlap{.}°05$ to provide sub-sampling of the point-spread function (PSF) perpendicular to the scan. By trailing the image, we obtained hundreds of astrometric measurements for each star, while drastically reducing systematics from geometric distortion, jitter, and PSF sampling, but the astrometric information is only available in a direction perpendicular to the trails. Ideally, we would have scanned the field in a direction that was perpendicular to the long axis of the parallax ellipse at the time of greatest parallactic offset, but a tradeoff must be made between available telescope roll,

parallax motion, and overlapping trails between stars. The optimized solution gave observations at the desired date but rotated by $27\rlap{.}°6$ from the ideal position angle, reducing the measurement sensitivity by a factor of 0.89. At this orientation, our measurements of the motions for cluster stars are more tangential than radial ($57\rlap{.}°4$ from radial).

The spatial scans produced useful trails for stars brighter than $V \lesssim 18.5$ mag. To characterize the stars associated with each trail requires a photometric catalog reaching at least this depth, and the *HST* direct images are far deeper. Given the sparse field, PSF-fitting photometry is unnecessary, and we produced catalogs from the direct images using aperture photometry ($0\rlap{.}''2376$ radius) derived with the APER routine (Landsman 1993). The *HST* catalogs were then merged with ground-based Strömgren photometry of the same field (Anthony-Twarog & Twarog 2000), which also reaches well below $V = 18.5$ mag. Using the same criteria as Anthony-Twarog & Twarog (2000), based upon the full Strömgren photometry, we characterized stars as cluster members or field stars (see Figure 2).

### 2.2. Southern Astrophysical Research (SOAR) Observations

Our *HST* spatial scans yield relative parallaxes, and these must be put in an absolute frame using distance estimates for the field stars along the sightline. The distance estimates are primarily based upon multi-band photometry of our field, but to supplement this information for a subset of stars, we obtained multi-object spectroscopy with the Goodman Spectrograph (Clemens et al. 2004) on the SOAR telescope, with a wavelength coverage of $\sim$350–580 nm. In practice, this yielded spectral classifications for only 14 of the 89 field stars used to determine the parallax absolute frame. For most of these 14 stars, the spectra reaffirmed the photometric characterization, but for a few, the spectroscopy allowed us to distinguish between multiple possibilities (i.e., dwarfs versus giants).
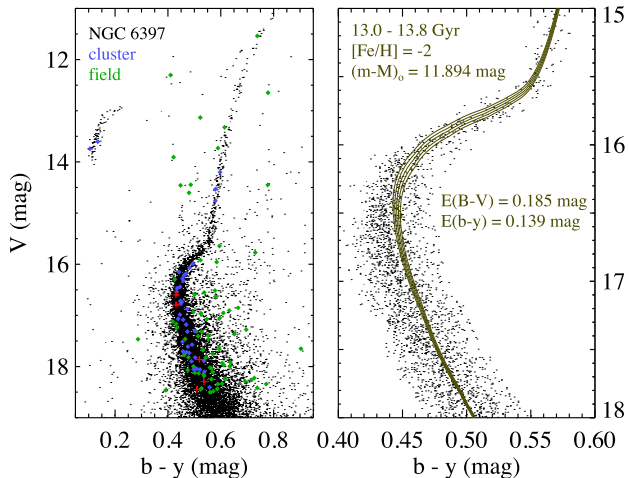
**Figure 2.** Left panel: the CMD for NGC 6397 (Anthony-Twarog & Twarog 2000). Stars with clean trails in the *HST* spatial scans are indicated in blue (cluster) and green (field), using the same membership criteria employed by Anthony-Twarog & Twarog (2000), based upon the full set of Strömgren photometry and indices. Red crosses indicate stars included in our cluster sample that appear to be outliers (see the text and Figure 4). Right panel: an expansion of the CMD at the MSTO, which is sensitive to age, showing only cluster members as designated in Anthony-Twarog & Twarog (2000). Isochrones (VandenBerg et al. 2014) are shown for a range of ages at the cluster metallicity ($[Fe/H] = -2.0$, $[\alpha/Fe] = +0.4$), the assumed extinction, and our derived distance modulus (labeled), with the $b - y$ color calibrated to match the base of the red giant branch. The locus is best matched by the 13.4 Gyr isochrone.

## 3. Analysis

The use of *HST* spatial scans to measure parallaxes was pioneered in Cepheid observations (e.g., Riess et al. 2014; Casertano et al. 2016). The technique is summarized in Riess et al. (2018 and references therein). Here, we briefly summarize the technique, along with the distinctions between our program and the Cepheid programs.

Each spatial scan produces trails that are nearly aligned with detector $Y$. Astrometric measurements are made along detector $X$ by fitting a position-dependent line-spread function to each 15 pixel minirow along a scan, excluding cosmic rays and detector artifacts, giving many measurements of $X$ as a function of $Y$ for each star. These relative detector coordinates are transformed to relative sky coordinates using a geometric distortion solution determined as in Bellini et al. (2011), including an empirically derived delta geometric distortion map (Casertano et al. 2016), with corrections for time-dependent plate-scale variations, frame-to-frame rotation, and rotation during an individual scan. The relative astrometry is registered using a 2D second-order polynomial that accounts for time-dependent distortions along the measurement direction, and measured relative to a reference line that contains the jitter history, length, and slope of the scan, constructed from the superposition of all time-aligned scan lines. A model is then fit simultaneously to the cluster and reference field stars, using for the latter photometric distance constraints derived by comparing our multi-band photometry to the stellar population along this sightline in the Besançon Model of the Galaxy (Robin et al. 2003). Synthetic Strömgren and *HST* photometry for the stars in the Besançon model was calculated using MARCS spectra (Gustafsson et al. 2008), supplemented by Castelli & Kurucz (2003) spectra at high temperatures. The stellar motions are modeled as the superposition of a relative proper motion

and parallax over five epochs (2 years), accounting for the projection of the parallax ellipse on detector $X$. In Figure 3, we show the parallax motions for representative cluster and field stars, as derived in one of the two bounding solutions discussed below.

Our program has several distinctions from the Cepheid programs. First, in the Cepheid programs, each image targets a single bright Cepheid and dozens of relatively faint field stars, necessitating the use of multiple filters to obtain the appropriate signal; the cross-registration of these distinct filters incurs a cost in the error budget. Here, each image targets multiple cluster stars of similar brightness to the field reference stars (see Figure 2), conveying the advantage that all scans are in a single filter (F606W). Second, in the Cepheid analysis, the reference frame is derived by comparing the field stars to a set of isochrones anchored to the Besançon model, providing a finer grid of stellar parameters than the model itself. Here, we have translated the Besançon model directly to synthetic *HST* and Strömgren photometry for comparison to the observations. The comparison to the Besançon model produces a probability distribution function (PDF) for the estimated distance to each field star. Where the PDF has multiple peaks, the first iteration of the analysis uses a prior spanning these peaks, and then subsequent iterations down-select to a single peak consistent with the previous solution. Third, the Cepheid analysis iteratively solves for the extinction along the sightline, using the Schlafly & Finkbeiner (2011) dust extinction map as a prior. Here, we rescale the extinctions in the Besançon model such that $E(B - V) = 0.185$ mag at the distance of NGC 6397, given the foundation of literature associated with the cluster; otherwise, the Besançon model would give a much lower value (0.141 mag) for this sightline at the cluster distance. In comparison to the Cepheids, the higher Galactic latitude of NGC 6397 puts nearly all of the stars in our sample outside of the thin disk, imposing essentially constant extinction. Fourth, the Cepheid programs have sampled 4–9 epochs per star, while here we have sampled 5 epochs. Fifth, we adopt a weak proper motion prior for the cluster stars, with a width of 15 km s$^{-1}$ in the resolution direction, and a mean proper motion of zero (we have no absolute proper motion reference). This prior constrains the inter-epoch alignment of the overall solution, but our derived proper motions and parallaxes come solely from our astrometric measurements. No such prior exists in the Cepheid programs. Finally, the Cepheid program images each have a single Cepheid, while our images have multiple cluster stars assumed to be at the same distance; we thus apply weights to account for fit quality when combining the individual cluster measurements into a single cluster distance. Specifically, we increase the errors for each cluster star such that $\chi^2 < 2$, and then weight each star in inverse proportion to its errors squared.

The level of precision we are seeking in our program is in a different regime than that in the Cepheid programs, making it sensitive to effects at the $\sim 2 \times 10^{-4}$ pix level, compared to $\sim 10^{-3}$ pix in the Cepheid programs. At this precision, our program has revealed a sensitivity to systematic uncertainties that currently dominate our analysis. We defer a more complete discussion of these systematics to a full-length paper (S. Casertano et al. 2018, in preparation). Here, we note that the solution changes significantly depending upon the samples employed in the analysis. Two solutions that bound the results are shown in Figure 4. In the left panel, the relative proper motion and astrometric parallax are shown for each of the 44
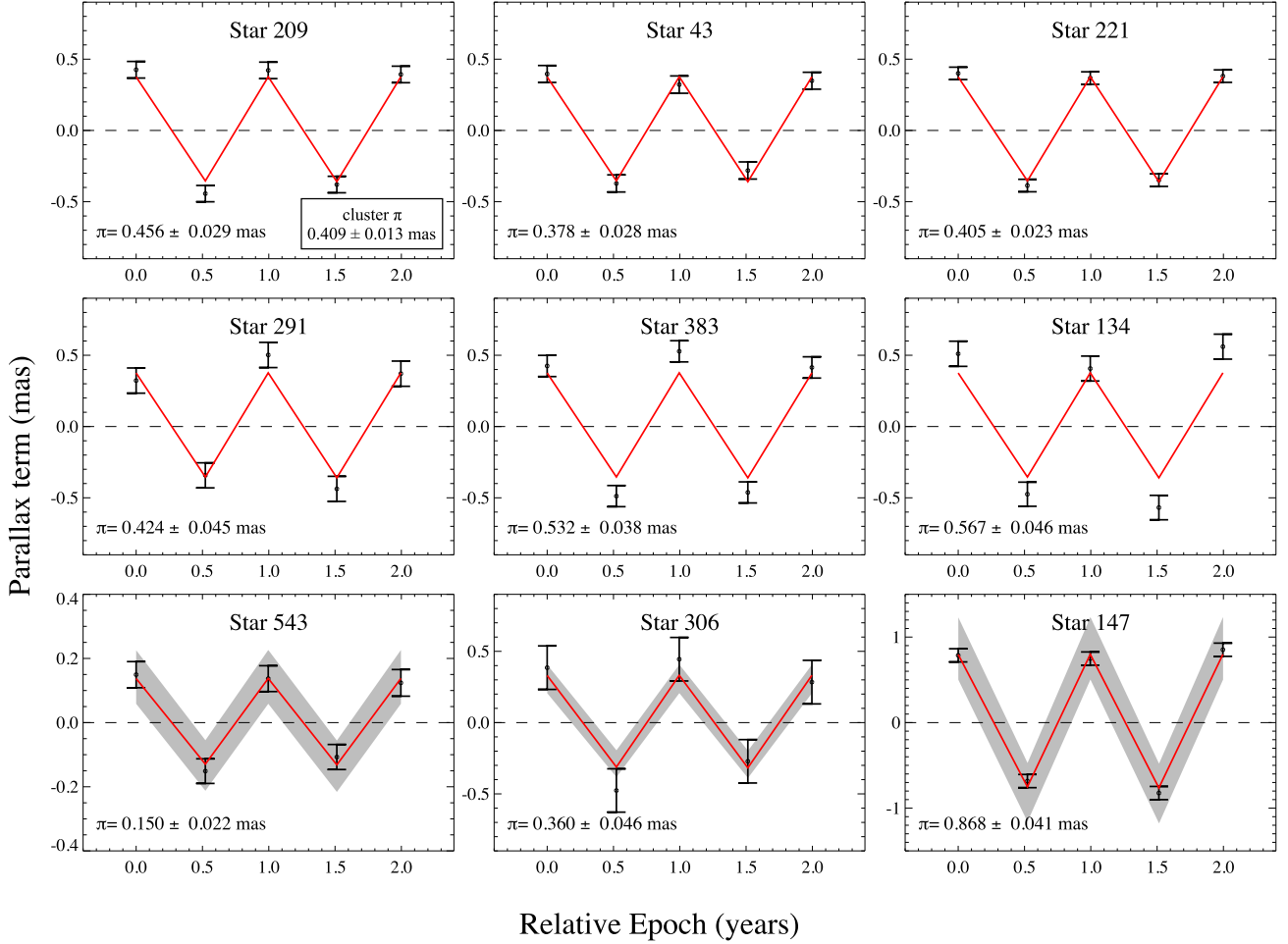
**Figure 3.** Top six panels: the proper motion subtracted 1D motions for six representative cluster stars, as observed over five epochs (2 years). These motions come from our analysis of the full cluster sample of 44 stars (left panel in Figure 4). The red line indicates the measured cluster parallax from the full solution that assumes all of the cluster stars are at the same distance, with all errors propagated. The individual parallaxes represent the pure astrometric measurement for each star in isolation. Bottom three panels: the same, but for three representative field stars from our sample of 89. The red line indicates the measured parallax for each field star, while the gray band indicates the photometric parallax with $2\sigma$ width.

stars in our cluster sample. Using the full sample, the cluster parallax is 0.409 mas, and the one-dimensional velocity dispersion is 6.2 km s$^{-1}$, although we note that the direction of our measurement is largely tangential (see Figure 1). There are several apparent outliers, despite the fact that they appear to be members in the Strömgren and *HST* photometry. If we median clip the sample at $2\sigma$ (green circle), this removes five outliers. The weighted average of the remaining 39 measurements, without re-running the full solution, gives a parallax of 0.411 mas, which is not significantly distinct from that in the full sample, although the velocity dispersion drops to 5.0 km s$^{-1}$. For comparison, the central velocity dispersion of NGC 6397 has been measured at 4.5 km s$^{-1}$, dropping to 2.2 km s$^{-1}$ in the outskirts (Meylan & Mayor 1991; see also Kamann et al. 2016). However, if we then reprocess the full solution with that reduced sample of 39 stars (right panel), the parallax increases to 0.428 mas—a change larger than that expected from the statistical errors or from the actual values of the individual parallaxes themselves. The velocity dispersion in this new solution is 4.5 km s$^{-1}$. These five outliers may be stars with undetected problems (e.g., contamination by a fainter star, unresolved binary), or they may not be true cluster members. A

subset might be legitimate measurements of cluster stars, because it is not unreasonable for one or two stars to scatter beyond $2\sigma$. Our preliminary result takes the midpoint of these two bounding cases, giving a cluster parallax of 0.418 mas, with a systematic uncertainty of 0.010 mas due to the dependency on the sample, and a statistical uncertainty of 0.013 mas, dominated by the correction to absolute parallax.

There is good agreement between our photometric priors and astrometric results for the field population, with half the sample agreeing at the $1\sigma$ level, and 70% of the sample agreeing at the $2\sigma$ level. However, there is an additional systematic uncertainty associated with the photometric parallax priors of the field reference stars, due to the extinction uncertainty along this sightline and the uncertainties in the absolute luminosities for the model stellar population. We can estimate this systematic error by shifting the distance moduli of the reference stars by +0.1 mag, which will have a larger impact on the parallax priors for the relatively nearby stars. For such a shift, the cluster parallax solution changes by −0.015 mas. Adding these systematics in quadrature, our systematic uncertainty for the cluster parallax
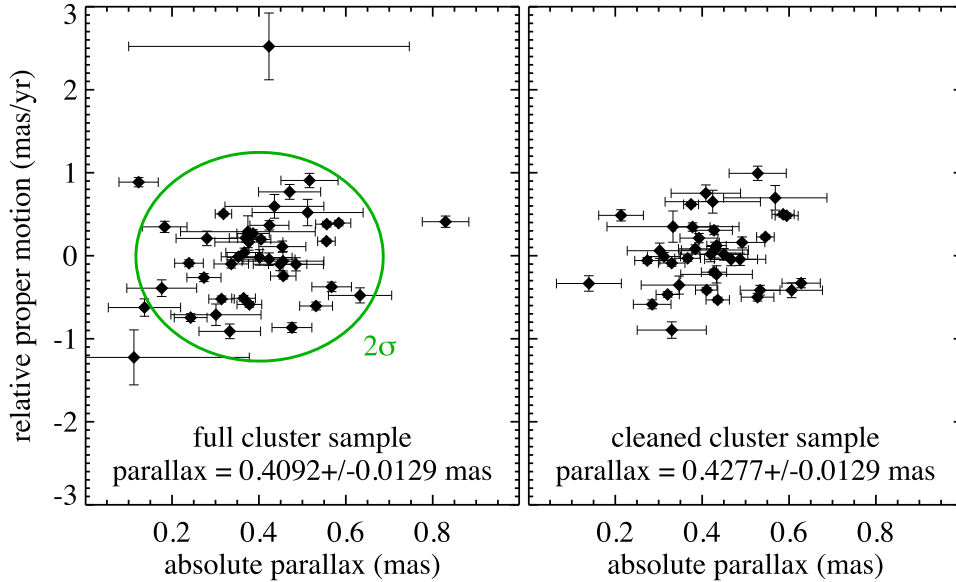
**Figure 4.** Left panel: individual measurements of proper motion and parallax for our full sample of 44 cluster stars (see Figure 2). For comparison, the ellipse axes give the 2σ variation in the measurements of proper motion and parallax, centered on the median value of each. Five stars fall outside of this ellipse. The parallax from this full sample is 0.4092 mas. The weighted average of the measurements here is not significantly changed if the outliers are removed. Note that the cluster parallax in the full solution propagates all errors, such that the cluster parallax uncertainty is larger than that one would expect from a weighted average of the individual measurements. Right panel: the full solution derived from 39 stars after removal of the five outliers. The result is an increased cluster parallax of 0.4277 mas, and the individual measurements have appreciably shifted with respect to the previous solution.

increases to 0.018 mas. The true distance modulus is $11.89 \pm 0.07 \pm 0.09$ mag ($2.39 \pm 0.07 \pm 0.10$ kpc).

## 4. Discussion

We have measured a trigonometric parallax of $0.418 \pm 0.013 \pm 0.018$ mas for the nearest metal-poor globular cluster, NGC 6397. The distance modulus, $11.89 \pm 0.07 \pm 0.09$ mag, is shorter than most measured previously, at the level of $1\sigma$–$2\sigma$ (cf. Reid & Gizis 1998; Gratton et al. 2003; Hansen et al. 2007), but consistent with a recent dynamical distance (Watkins et al. 2015). We note that new subdwarf fits to NGC 6397 also yield a relatively short distance (D. VandenBerg et al. 2018, in preparation) that is consistent with our results.

With the upcoming catalog from *Gaia* Data Release 2, we will have an independent measurement of the NGC 6397 distance for comparison, to the extent that the *Gaia* results for individual cluster stars can be combined, accounting for the correlated errors on the scale of the cluster. Furthermore, the *Gaia* results can be used to augment the *HST* analysis by redefining the distance priors for the reference field stars. The combined measurement should yield a parallax uncertainty at the level of ~1%.

Relative cluster ages are generally measured in two ways: the luminosity difference between the horizontal branch and the MSTO increases at older ages, and the color difference between the MSTO and the base of the red giant branch decreases at older ages. Combining these methods, VandenBerg et al. (2013) found an age of 13.0 Gyr for NGC 6397. The MSTO absolute luminosity is also an absolute age indicator, when compared to isochrones at fixed distance. In Figure 2, we show the VandenBerg et al. (2014) isochrones translated into the frame of the Anthony-Twarog & Twarog (2000) photometry, using our assumed extinction and derived distance. The *V* luminosities are those in the VandenBerg et al. (2014) library; the $b - y$ colors come from synthetic photometry, using

MARCS spectra (Gustafsson et al. 2008) and the temperatures and gravities along the isochrones. The $b - y$ transformation has been calibrated to retain the MSTO color, but match the observed color difference between the MSTO and the base of the red giant branch. The comparison to the isochrones implies an absolute cluster age of 13.4 Gyr.

There are significant statistical and systematic uncertainties when deriving an absolute age. The MSTO absolute luminosity changes by ~0.1 mag per Gyr at old ages, such that the statistical (0.07 mag) and systematic (0.09 mag) uncertainties in distance modulus correspond to 0.7 and 0.9 Gyr in age. Modern isochrone libraries (e.g., VandenBerg et al. 2014; Choi et al. 2016; Marigo et al. 2017) agree at the level of ~0.06 mag for the absolute MSTO luminosity at a particular chemical composition, giving another of 0.6 Gyr. Oxygen abundance uncertainties of ~0.2 dex correspond to an age uncertainty of 0.6 Gyr. These systematics combine for a total uncertainty of 1.2 Gyr in absolute age.

Schmidt Telescope on Palomar Mountain and the UK Schmidt Telescope. The plates were processed into the present compressed digital form with the permission of these institutions. The Second Epoch Survey of the southern sky was made by the Anglo-Australian Observatory with the UK Schmidt Telescope. Plates from this survey have been digitized and compressed by the STScI. The digitized images are copyright 1993-2000 by the Anglo-Australian Observatory Board, and are distributed herein by agreement.

## ORCID iDs

T. M. Brown ⓘ https://orcid.org/0000-0002-1793-9968

## References

Anthony-Twarog, B. J., & Twarog, B. A. 2000, AJ, 120, 3111
Anthony-Twarog, B. J., Twarog, B. A., & Suntzeff, N. B. 1992, AJ, 103, 1264
Bedin, L. R., Maurizio, S., Giampaolo, P., et al. 2009, ApJ, 697, 965
Bellini, A., Anderson, J., & Bedin, L. R. 2011, PASP, 123, 622
Bruzual, G., & Charlot, S. 2003, MNRAS, 344, 1000
Cacciari, C., & Clementini, G. 2003, LNP, 635, 105
Casertano, S., Riess, A. G., Anderson, J., et al. 2016, ApJ, 825, 11
Castelli, F., & Kurucz, R. L. 2003, in IAU Symp. 210, Modeling of Stellar Atmospheres, ed. N. Piskunov, W. W. Weiss, & D. F. Gray (Cambridge: Cambridge Univ. Press), A20
Choi, J., Dotter, A., Conroy, C., et al. 2016, ApJ, 823, 102
Clemens, J. C., Crain, J. A., & Anderson, R. 2004, Proc. SPIE, 5492, 331
Dias, W. S., Alessi, B. S., Moitinho, A., & Lépine, J. R. D. 2002, A&A, 389, 871
Gratton, R. G., Bragaglia, A., Carretta, E., et al. 2003, A&A, 408, 529
Gustafsson, B., Edvardsson, B., Eriksson, K., et al. 2008, A&A, 486, 951
Hansen, B. M. S., Anderson, J., Brewer, J., et al. 2007, ApJ, 671, 380
Hansen, B. M. S., Richer, H. B., Fehlman, G. G., et al. 2004, ApJS, 155, 551
Harris, W. E. 1996, AJ, 112, 1487
Kamann, S., Husser, T.-O., Brinchmann, J., et al. 2016, A&A, 588, A149
Kraft, R. P., & Ivans, I. I. 2003, PASP, 115, 143
Landsman, W. B. 1993, in ASP Conf. Ser. 52, Astronomical Data Analysis Software and Systems II, ed. R. J. Hanish, R. J. V. Brissenden, & J. Barnes (San Francisco, CA: ASP), 246
MacKenty, J. W. 2012, Proc. SPIE, 8442, 84421V
Marigo, P., Girardi, L., Bressan, A., et al. 2017, ApJ, 835, 77
Meylan, G., & Mayor, M. 1991, A&A, 250, 113
Pancino, E., Bellazzini, M., Giuffrida, G., & Marinoni, S. 2017, MNRAS, 467, 412
Piotto, G., Milone, A. P., Bedin, L. R., et al. 2015, AJ, 149, 91
Prusti, T. 2012, Gaia Intermediate Data Release Scenario, GAIA-CG-PL-ESA-TJP-011-01
Reid, I. N., & Gizis, J. E. 1998, AJ, 116, 2929
Riess, A. G., Casertano, S., Anderson, J., MacKenty, J., & Fillippenko, A. V. 2014, ApJ, 785, 161
Riess, A. G., Casertano, S., Yuan, W., et al. 2018, ApJ, in press (arXiv:1801.01120)
Robin, A. C., Reylé, C., Derrière, S., & Picaud, S. 2003, A&A, 409, 523
Schlafly, E. F., & Finkbeiner, D. P. 2011, ApJ, 737, 103
Schlegel, D. J., Finkbeiner, D. P., & Davis, M. 1998, ApJ, 500, 525
Soderblom, D. R., Nelan, E., Benedict, G. F., et al. 2005, AJ, 129, 1616
van der Marel, R. P., & Anderson, J. 2010, ApJ, 710, 1063
van Leeuwen, F. 2009, A&A, 497, 209
van Leeuwen, F., Vallenari, A., Jordi, C., et al. 2017, A&A, 601, 19
VandenBerg, D. A., Bergbusch, P. A., Ferguson, J. W., & Edvarddson, B. 2014, ApJ, 794, 72
VandenBerg, D. A., Brogaard, K., Leaman, R., & Casagrande, L. 2013, ApJ, 775, 134
Watkins, L. L., & van der Marel, R. P. 2017, ApJ, 839, 89
Watkins, L. L., van der Marel, R. P., Bellini, A., & Anderson, J. 2015, ApJ, 812, 149